SIMULATIVE MODELING AND ANALYSIS OF THERMO-MECHANICAL AND TRIBOLOGICAL PROCESSES IN ELECTRO-CHEMICALLY RIFLED FIREARM BARRELS WITH ANODIZED AND CHROME COATINGS

Ventsislav Dimitrov[1] [https://orcid.org/0009-0006-9667-8028], Veselina Krasimirova Dimitrova[2] [https://orcid.org/0009-0001-0157-1775], Galya Stoyanova Zdravcheva[3] [https://orcid.org/0009-0009-3159-5514]
[1,2]Department MEMETE, Faculty of Engineering and Pedagogy of Sliven, Technical University of Sofia, Bulgaria
[3]Department Energy and Mechanical Engineering, Technical College - Sofia, Technical University of Sofia, Bulgaria
Emails: vpdd_acad@tu-sofia.bg, vkdd_acad@tu-sofia.bg

Abstract - This study presents original simulation modelling of thermo-mechanical and tribological processes in firearms manufactured via Electro-Chemical Rifling (ECR) followed by anodized and chrome coatings. Employing the finite element method (FEM), the study investigates the influence of material properties and dynamic loading conditions on the thermal behaviour and wear mechanisms of aluminium and steel firearms. Results demonstrate that chrome coatings are approximately ten times thicker than anodic oxide layers, possess 3.2 times greater hardness, and reduce the dynamic coefficient of friction by an average of 16%. The allowable number of operational cycles for chrome-plated steel firearms exceeds that of hard-anodized aluminium counterparts by a factor of 12. Deformations under identical conditions remain below maximum permissible limits, with steel firearms exhibiting approximately 2.37 times less deformation than aluminium firearms. These quantitative findings provide significant insights into the interaction between materials, coatings, and dynamic operational stresses, offering potential for optimising manufacturing processes and substantially enhancing the durability and reliability of firearms.

Keywords: Electro-chemical rifling (ECR), Under-barrel grenade launcher, Firearms, Thermal analysis, Ballistic parameters, Tribology, Wear resistance, Anodized coatings, Chrome coatings, Dynamic loading, Hardness, Friction coefficient, Heat flux.

1. Introduction

The internal ballistic process occurring within a firearm barrel encompasses a complex interplay of kinematic, solid mechanical, fluid dynamic, thermal, and powder combustion phenomena [1–5]. During the extremely rapid combustion of the propellant charge, a transient build-up of high-pressure, high-temperature gases takes place over a timescale of only a few milliseconds.

This sudden overpressure exerts force upon the projectile, initiating its forward motion through the barrel. The acceleration phase is accompanied by intense frictional interaction between the projectile and the inner barrel surface, as well as a pronounced increase in temperature due to extreme thermal loading conditions [6–8].

The principal ballistic parameters function as essential input variables for the finite element simulation model [9,10]. It is assumed that the material of the analysed component—typically steel or aluminium—exhibits ductile behaviour and follows an idealised linear-elastic, linear-plastic stress–strain relationship. This constitutive model accounts for material strain hardening, plastic deformation history, and variations in boundary stress values (fig.1,a) [1,11].

The stages of the simulation modelling process are illustrated in Figure 1b.

The rifled firearm barrel analysed in this study is schematically depicted in fig. 2. Precise drawings and dimensional data are not disclosed due to proprietary company restrictions.

The barrel was manufactured using Electro-Chemical Rifling (ECR) [12–15] under the following process parameters: current (I) ≈ 950 A, time (t) ≈ 176 s, pressure (P) ≈ 22 bar, and voltage (U) ≈ 7 V.

dx.doi.org/10.17683/ijomam/issue21.7

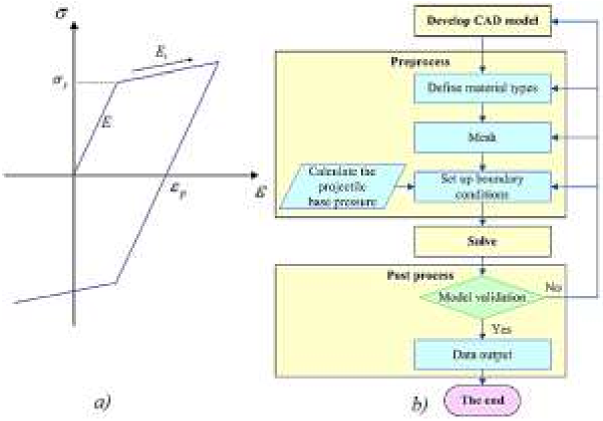

Figure 1: Stress–strain relationship of an elastic–plastic material and schematic of the analysis process [1, 9, 11]: (a) Elastic–plastic constitutive material model; (b) Full simulation workflow.

Figure 2: Cross-section of a rifled weapon barrel

The surface quality was assessed based on surface roughness, defined by the height parameter and the arithmetic mean deviation of the profile, with a measured value of Ra = 0.8 μm [16,17].

The chemical composition and mechanical properties of the materials used for the ECR-processed firearm barrels correspond to aluminium alloy EN AW-7075 and steel grade 30CrNiMgVA. Following rifling, the barrels were subjected to anodising and chromium electroplating.

The chromium coating thickness was found to be approximately ten times greater than that of the oxide layer, with a hardness 3.2 times higher and a dynamic coefficient of friction (μ) approximately 16% lower, on average.

Based on the recorded linear and volumetric wear rates, the maximum permissible number of operational cycles was determined to be approximately $n_{Fe} \approx 12{,}000$ for chromium-plated steel barrels, compared to $n_{Al} \approx 1{,}000$ for hard-anodised aluminium barrels.

2. Ballistic Characteristics

The motion of the projectile within the barrel is governed by the principles of interior ballistics [18–20]. The primary parameters evaluated include: barrel pressure P [MPa], projectile acceleration a [m/s^2], angular velocity ω [rpm], temperature T [°C], and projectile trajectory as a function of time t [μs]. These ballistic parameters serve as essential input data for the finite element simulation modelling [21–23].

It was established that the peak values of the internal ballistic parameters occur in regions located approximately 210–225 mm from the muzzle, corresponding to the onset of the rifled portion of the bore. Beyond this point—upon projectile exit—the motion transitions to the regime of exterior ballistics.

The values of the ballistic parameters, as influenced by specific operational, technological, and geometrical constraints of the components, were derived through a series of single-factor experimental investigations. These studies isolated individual variables to quantify their influence under controlled conditions. The results are summarised in Table 1 and are graphically presented in fig.3 to 5.

Table 1. Ballistic characteristics

Exper. №	Ballistic characteristics							Law
	Time t [μs]	Dist. from the bottom L [mm]	Velocity V [m/s]	Pressure P [MPa]	Accelerat. [m/s^2]	Angular ω velocity [rpm]	Temperat. T [°C]	
1	10	25	5	10	5	0	20	Internal ballistics
2	50	35	80	120	100	20000	25	
3	100	55	205	275	200	29000	260	
4	150	75	285	375	295	30000	185	
5	200	100	375	255	200	35000	115	
6	250	125	445	195	160	36000	120	
7	300	150	500	135	150	45000	100	
8	350	175	530	110	145	45000	95	
9	400	205	540	90	145	47500	85	
10	450	235	545	75	135	47000	80	
11	510	280	549	60	130	48000	50	
12	550	310	545	0	20	48000	0	External ballistics
13	600	345	540	0	30	47500	0	
14	650	380	535	0	25	48000	0	
15	700	415	535	0	15	47500	0	
16	750	455	535	0	20	48000	0	

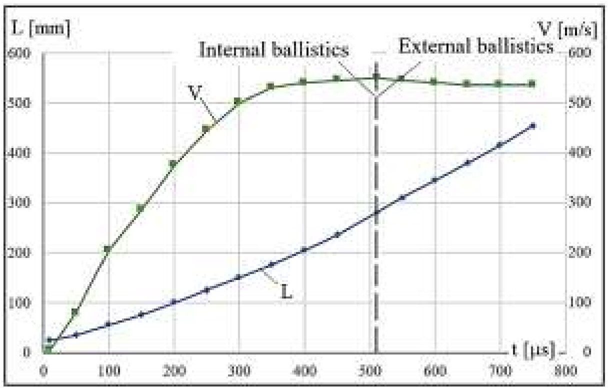

Figure 3: Dependence of distance L [mm] and velocity V [m/s] on time t [μs].

The results have been idealised, assuming identical ballistic parameter values for both materials. This approach guarantees consistency in the initial conditions for the subsequent comparative analysis based on simulation modelling.

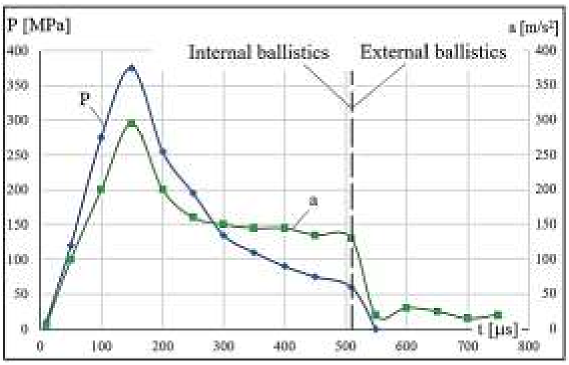

Figure 4:Dependence of pressure P [MPa] and acceleration a [m/s²] on time t [µs].

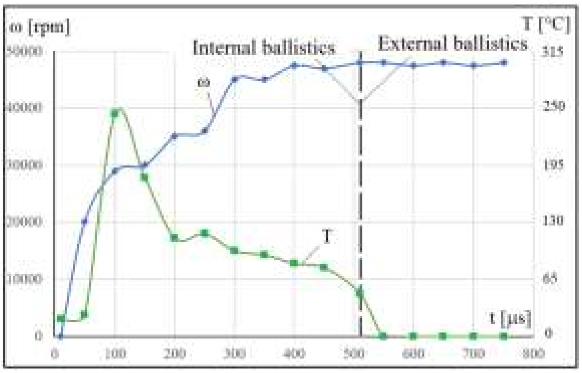

Figure 5: Dependency of angular velocity ω [rpm] and temperature T [°C] on time t [µs]

It is important to note that, for the purposes of consistency in comparative analysis, the ballistic input parameters were idealised and assumed identical for both material types. While this approach ensures uniform boundary conditions and facilitates direct comparison, it also introduces certain limitations. In real-world applications, variations in material properties, surface treatments, and manufacturing tolerances may lead to deviations in ballistic behaviour. Therefore, the presented results should be interpreted within the context of this assumption, and future studies should consider integrating more case-specific ballistic inputs for higher accuracy.

3. Simulation Modeling

Simulation modelling was performed using the Simulation application within the CAD system SolidWorks. Separate fluid (Flow Simulation) and thermal (Thermal Simulation) analyses were carried out, alongside a comprehensive strength-deformation assessment via the finite element method, which accounted for mechanical, thermal, and fluidic loads. The analysis focused on von Mises stress, σ [MPa], and deformation (URES), f [mm]. The behaviour of the barrel-projectile system was investigated for two distinct material types.

While numerous studies have investigated electrochemical machining and thermal behavior in firearm components, few have combined thermo-fluid-structural simulations in the context of ECR with different coatings. For instance, Sopok et al. [12] and Sun et al. [4] examined thermal and mechanical wear in gun barrels, but lacked integrated FEM analysis. Similarly, Deng et al. [9] performed transient FEM modelling of internal ballistics, yet did not address coating effects. Compared to these works, the present study offers a more comprehensive approach by simultaneously evaluating thermal gradients, fluid flow, and deformation behavior for both anodized and chrome-plated barrels under identical ballistic conditions. This integrated analysis provides a novel perspective on the material–coating interaction and offers practical implications for design and durability improvement.

A mesh independence study was conducted to ensure the reliability of the simulation results. Two different mesh densities were tested, and key output parameters such as maximum von Mises stress, total deformation (URES), and temperature distribution were compared. The variation in results between the fine and medium mesh was found to be within 1.5%, indicating that the selected mesh resolution provides accurate and stable predictions without excessive computational cost. As such, the medium-density mesh was adopted for the final simulations.

The simulation methodology followed a structured sequence of stages [24–26], beginning with precise parameterization. This included the definition of key material properties such as elastic modulus, density, and Poisson's ratio (μ). The analysed materials were assumed to be ductile and to conform to an idealized linear-elastic, linear-plastic behavior model. Factors such as work hardening, plastic deformation history, and stress limit variations were considered. The Maxwell–Huber–Hencky–von Mises yield criterion was employed throughout the analysis.

- setting geometric constraints on the three-dimensional model of the component, using a set of modifiers that physically express the removal of degrees of freedom. A mandatory condition for every model is the presence of an area with zero displacement, i.e., a fixed (immovable) support.
- after defining the constraints, the system requires the application of a load, realized through pressure on the internal surface of the component.
- validating the model by selecting the discretization and mesh shape.

For both material types—steel 30CrNiMgVA with a deposited chromium coating, and aluminum EN AW-7075 (ISO AlZn5.5MgCu) with a hard anodized coating—the corresponding material parameters were incorporated into the simulation. The input values for the parameters required in the simulation analyses are detailed in Table 2.

Table 2. Material Properties

EN AW-7075 (ISO AlZn5,5MgCu)

Property	Value	Units
Elastic Modulus	7.2e+10	N/m^2
Poisson's Ratio	0.33	N/A
Shear Modulus	2.69e+10	N/m^2
Mass Density	2810	kg/m^3
Tensile Strength	570000000	N/m^2
Compressive Strength		N/m^2
Yield Strength	505000000	N/m^2
Thermal Expansion Coefficient	2.36e-05	/K
Thermal Conductivity	130	W/(m·K)
Specific Heat	960	J/(kg·K)
Material Damping Ratio		N/A

30CrNiMgVA

Property	Value	Units
Elastic Modulus	2.1e+11	N/m^2
Poisson's Ratio	0.28	N/A
Shear Modulus	7.9e+10	N/m^2
Mass Density	7800	kg/m^3
Tensile Strength	1250000000	N/m^2
Compressive Strength		N/m^2
Yield Strength	1050000000	N/m^2
Thermal Expansion Coefficient	1.1e-05	/K
Thermal Conductivity	38	W/(m·K)
Specific Heat	440	J/(kg·K)
Material Damping Ratio		N/A

hard anodized coating

Property	Value	Units
Elastic Modulus	8.42e+10	N/m^2
Poisson's Ratio	0.707	N/A
Shear Modulus	2.69e+10	N/m^2
Mass Density	2320	kg/m^3
Tensile Strength	465000000	N/m^2
Compressive Strength		N/m^2
Yield Strength	418000000	N/m^2
Thermal Expansion Coefficient	13.8e-05	/K
Thermal Conductivity	63	W/(m·K)
Specific Heat	1300	J/(kg·K)
Material Damping Ratio		N/A

chromium coating

Property	Value	Units
Elastic Modulus	1.5e+11	N/m^2
Poisson's Ratio	0.046	N/A
Shear Modulus	7.9e+10	N/m^2
Mass Density	6900	kg/m^3
Tensile Strength	1123000000	N/m^2
Compressive Strength		N/m^2
Yield Strength	1082000000	N/m^2
Thermal Expansion Coefficient	8.9e-05	/K
Thermal Conductivity	165	W/(m·K)
Specific Heat	653	J/(kg·K)
Material Damping Ratio		N/A

The fluid simulation model was conducted assuming a constant ambient temperature of $\vartheta_a mb$ = 20 °C, with no interaction between the component and any external cooling medium. The fluid simulation model is visualised in Figure 6.

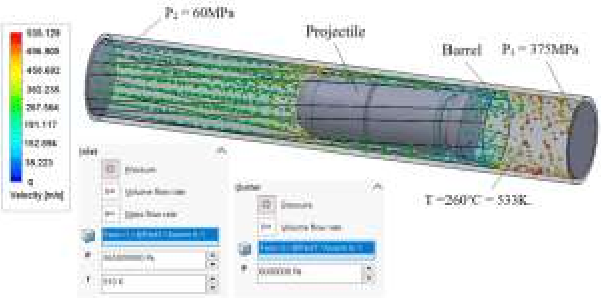

Figure 6: Fluid simulation

The pressure at the system inlet was set to P_1 = 375 MPa, and at the outlet to P_2 = 60 MPa, with an operating temperature of T = 260 °C (533 K). The maximum fluid velocity obtained from the simulation was V = 535 m/s, deviating by only 2.55% from the experimentally measured value of 549 m/s. This close correlation confirms the reliability and accuracy of the fluid simulation performed using the finite element method.

The primary objective of the thermal analysis is to investigate heat distribution within the zone characterised by extreme ballistic parameters and wear.

For each material type, temperature, temperature gradients, and heat flux are graphically presented in Figures 7–10.

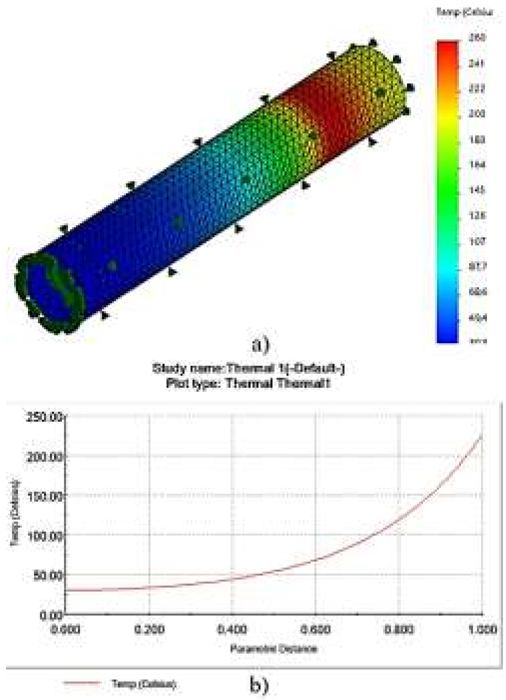

Figure 7: Thermal simulations of the aluminium hard-anodized component: (a) Heat exchange distribution; (b) Temperature profile along the Z-axis.

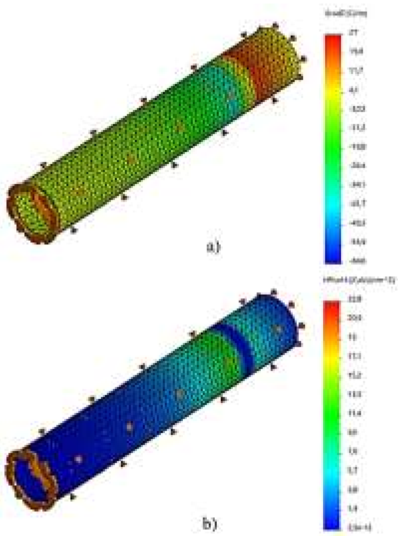

Figure 8: Thermal simulations of the aluminium hard-anodized component: (a) Temperature gradient along the Z-axis; (b) Heat flux distribution.

The results present temperature field isolines with a high density near the rifling zone, where the maximum thermal load is observed. Moving away from this region, the temperature decreases sharply. The longitudinal temperature gradient along the Z-axis was found to be 109°C/cm for steel components, which is approximately 4.3 times higher than the 27°C/cm observed for aluminum.

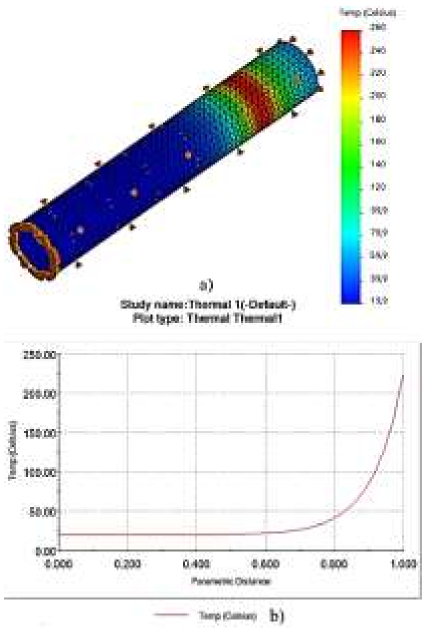

Figure 9: Thermal simulations of the steel chromium-plated component: (a) Heat exchange; (b) Temperature profile along the Z-axis.

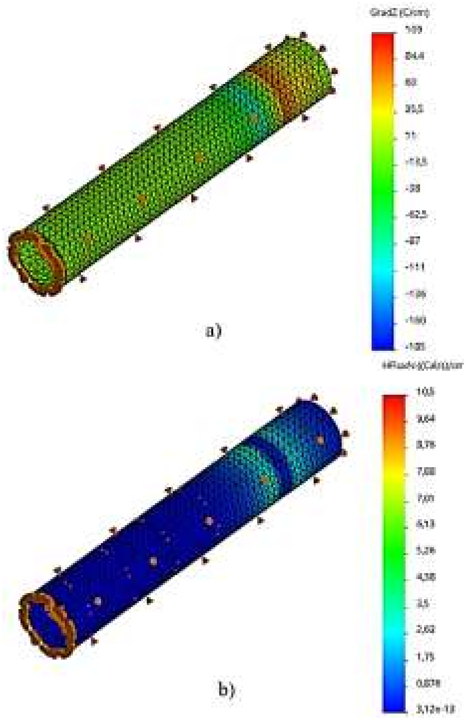

Figure 10: Thermal simulations of the steel chromium-plated component: (a) Temperature gradient along the Z-axis; (b) Heat flux distribution.

This suggests that steel barrels are subjected to more intense heat flux, with greater energy transfer per unit time and surface area. However, the heat flux in aluminum barrels was 56% higher than in steel, indicating that aluminum dissipates heat significantly faster under the same thermal load.

These findings are largely attributed to the higher heat transfer coefficient of the oxide coatings (13.6 K^{-1}) compared to that of the chromium coatings (0.9 K^{-1}), as well as the superior thermal resistance of chromium coatings (163 W/(m·K)) relative to oxide coatings (63 W/(m·K)). The analysis indicates that aluminum barrels possess superior thermal conductivity, while steel barrels exhibit greater durability and thermal resistance under equivalent operational conditions.

The strength-deformation analysis was conducted with geometric constraints applied to the barrel, eliminating all degrees of freedom, and a load corresponding to the maximum pressure of P = 375 MPa was applied. Moreover, data derived from the fluid and thermal simulations were incorporated into the analysis to enhance accuracy, as illustrated in fig. 11a and fig.11b.

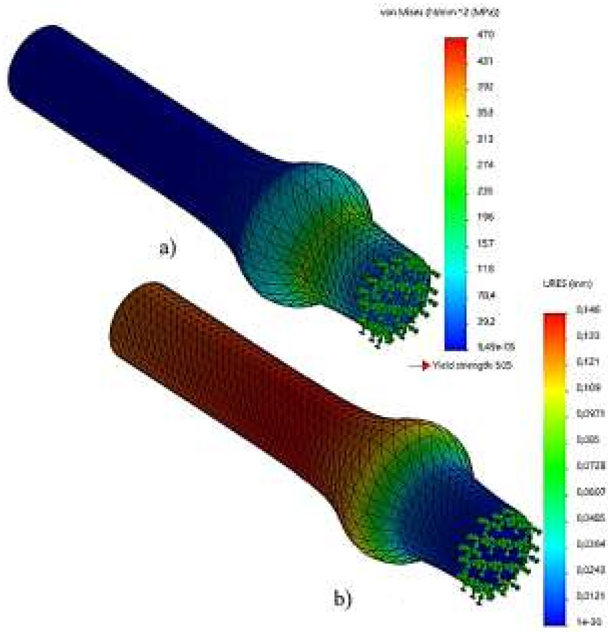

Figure 11: Strength-deformation analysis of the hard-anodized aluminum barrel: (a) von Mises stress [MPa], (b) deformation (URES) [mm].

Regarding the von Mises stress σ [MPa], localized regions exhibiting stresses marginally above the allowable limits were observed; however, the exceedance did not surpass 0.5%, and was noted exclusively in steel barrels.

This deviation can be regarded as normal, considering the complex geometry of the components. For both material types, regions of maximum stress are located within the zones of extreme loading and diminish sharply with increasing distance from these zones. This observation corroborates prior expectations regarding the location of critical sections, which were based on operational experience.

The trend depicted in Figure 12 clearly demonstrates that, despite being subjected to the most intense mechanical and thermal loads, steel barrels accommodate higher stresses while exhibiting lower deformation compared to aluminum barrels.

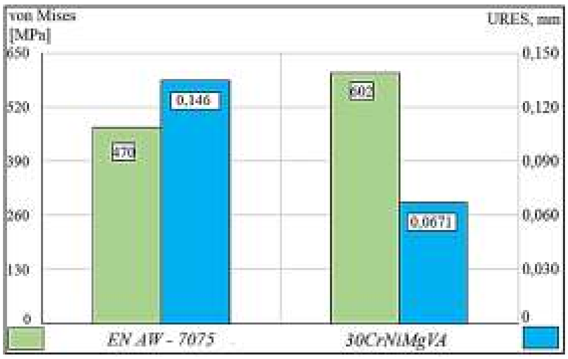

Figure 12: Strength-deformation analysis.

The results align with the linear and volumetric wear data, thereby further validating the performance and integrity of the applied coatings.

To assess the reliability of the numerical results, an uncertainty analysis was performed. The deviation between the simulated maximum fluid velocity (535 m/s) and the experimentally measured value (549 m/s) was calculated to be 2.55%. This margin was used as a reference to estimate the uncertainty in other simulation outputs. Across all major parameters—including temperature distribution, von Mises stress, and total deformation (URES)—the estimated uncertainty remained within ±3%. These values are considered acceptable for engineering applications and support the validity of the presented simulation results.

4. Conclusions

Based on the conducted investigations and the simulation modelling of the processes occurring within firearm barrels featuring anodised and chromium-plated coatings, the following key conclusions have been drawn:

A series of one-factor, single-parameter experimental studies yielded values for the critical ballistic parameters: barrel pressure P [MPa], projectile acceleration a [m/s^2], angular velocity ω [rpm], temperature T [°C], and trajectory as a function of time t [μs].

For modelling consistency, the ballistic input parameters were idealised and assumed identical for both material types, ensuring uniform initial conditions in the simulations.

The fluid simulation model was executed at a constant ambient temperature of ϑ_{amb} = 20°C, with no interaction with any external cooling agent.

The applied inlet pressure was P_1=375 MPa, and the outlet pressure was P_2=60 MPa, with an initial working temperature of T=260°C (533 K).

The simulation results demonstrated high fidelity, with the maximum fluid velocity V=535 m/s deviating by only 2.55% from the experimentally obtained value V=549 m/s.

The thermal simulation was carried out under steady-state conductive heat transfer conditions. Material- and coating-specific thermal conductivity coefficients were applied, with heat dissipation constrained to a convective boundary layer around the barrel surface.

Isothermal field plots revealed a high density of thermal isolines near the onset of rifling, confirming this zone as the area of peak thermal stress. Temperature values decline sharply along the barrel axis beyond this region.

The longitudinal temperature gradient along the Z-axis was determined to be 109°C/cm for steel barrels and 27°C/cm for aluminium barrels - indicating that steel exhibits a 4.3 - fold higher gradient.

The heat flux in aluminium barrels was calculated to be 56% higher than in steel barrels, signifying that aluminium dissipates heat approximately 56% more rapidly than steel under identical loading conditions.

A full strength-deformation analysis was performed via the finite element method (FEM), integrating thermal, fluid, and structural loads. The simulation included the mechanical and physical properties of the respective coatings.

Under identical loading conditions, all observed deformation values URES\text{URES}URES [mm] remained below the permissible mechanical limits, ensuring process stability. Notably, steel barrels deformed approximately 2.37 times less than aluminium barrels.

The findings conclusively demonstrate that chromium coatings provide superior load-bearing capacity and result in significantly lower deformation compared to oxide coatings.

Acknowledgements

The authors would like to thank the Research and Development Sector at the Technical University of Sofia for the financial support.

The authors also wish to thank Arsenal JSC – Kazanlak for the financial support, which enabled the present research.

References

[1] Ahmad, N.A., Samion, S., Rahim, E. Abd., Jamir, M.R. Mohd. (2020). Environmentally approach for enhancing tribological characteristics in metal forming: A review. Jurnal Tribologi. Vol. 26, Pp. 37-59;

[2] Alam, F., Kumar, A., Patel, A., Sharma, R., Balani, K. (2015). Processing, characterization and fretting wear of chromium oxide and silver nanoparticles reinforced ultra high molecular weight polyethylene biopolymer nanocomposite. JOM: the journal of the Minerals, Metals & Materials Society. Vol. 67. doi: 10.1007/s11837-015-1358-z

[3] Pattavanitch, J., Hinduja, S., Atkinson, J. (2010). Modelling of the Electrochemical Machining process by the Boundary Element Method. CIRP Annals-Manufacturing Technology. Vol. 59. Pp. 243-246. doi: https://doi.org/10.1016/j.cirp.2010.03.072

[4] Sun, C.H., Zhu, D., Li, Z.Y., Wang, L. (2006). Application of FEM to tool design for electrochemical machining freeform surface. Finite Elements in Analysis and Design. Vol. 43. Pp. 168-172. doi: https://doi.org/10.1016/j.finel.2006.08.004

[5] Tang, L., Feng, X., Zhai, K.G. (2019). Gap flow field simulation and experiment of electrochemical machining special-shaped inner spiral tube. Int. J. Adv. Manuf. Technol. Vol.100. Pp. 2485–2493. https://doi.org/10.1007/s00170-018-2865-1

[6] Conev, C., Karadzhov, T. (2021). Experimental Determination of the Powder Quantity in the Ignition Cartridge for the Reusable Training-Practice Mortar Round for Firing on Short Distances. Environment. Technology. Resources. Proceedings of the International Scientific and Practical Conference. Vol. 3. Pp. 45-48. doi: https://doi.org/10.17770/etr2021vol3.6575

[7] Kalev, K. (2015). Analytical Determination of Pressure in the Gun Barrel taking into Account the Wear. Greener and Safer Energetic and Ballistic Systems.

[8] Kalev, K. (2020). Strength Calculation of Shell Components of the 120-mm Multiple Use Short-Range Training Mortar Ammunition. International Conference Knowledge-based Organization. Vol.20. Pp. 120-125 doi: https://doi.org/10.2478/kbo-2020-0125K.

[9] Deng, S., Sun, H.K., Chiu, C-J. Chen, K.C. (2014). Transient finite element for in-bore analysis of 9 mm pistols. Applied Mathematical Modelling. Vol. 38. Pp. 2673–2688. doi: https://doi.org/10.1016/j.apm.2013.10.071

[10] Demirtas, H., Yilmaz, O., Kanber, B. (2021). A simplified mathematical model development for the design of free-form cathode surface in electrochemical machining. Materials and Manufacturing Processes. Vol. 21. Pp. 39-47. doi: 10.1080/10910344.2016.1275192

[11] Babaei, H., Malakzadeh, M., Asgari H. (2015). Stress Analysis of Gun Barrel Subjected to Dynamic Pressure. International Journal of Mechanical Engineering and Applications. Vol.3. Pp. 71-80 doi: 10.11648/j.ijmea.20150304.14

[12] Sopok, S., Rickard, C., Dunn, S. (2005). Thermal-chemical-mechanical gun bore erosion of an advanced artillery system part one: theories and mechanisms. Wear. Vol. 258. Pp. 659-670. doi: https://doi.org/10.1016/j.wear.2004.09.031

[13] Qu NS, Fang XL, Zhang YD, Zhu D. (2013.) Enhancement of surface roughness in electrochemical machining of Ti6Al4V by pulsating electrolyte. Int J Adv Manuf Technol 69(9–12). Pp.2703–270 doi: https://doi.org/10.1007/s00170-013-5238-9

[14] Yang, F., Zhang, J., Guo, C. (2020). Investigation of electrochemical machining for gradual change special-shaped deep spiral hole based on COMSOL. Int J Adv Manuf Technol. Vol.108. Pp. 2717–2725. doi: https://doi.org/10.1007/s00170-020-05581-7

[15] Yildiz, Y. (2021). 3D finite element analysis and mathematical modeling for estimation of material dissolution rate in the electrochemical machining processes. Journal of Solid State Electrochemistry. Vol. 25. Pp. 2249–2265. doi: https://doi.org/10.1007/s10008-021-04994-y

[16] Mahayuddin, N., Wahab, J.A., Salleh, M. A. A. M., Roduan, S. F., Chen, H. K. (2020). Surface texturing method and roughness effect on the substrate performance: A short review. Jurnal Tribologi. Vol. 27. Pp. 8-18.

[17] Kalev, K. (2014). Influence of the bore geometry change on the ballistic parameters of the gun barrel, NMU "Vasil Levski", Faculty "Artillery, Air Defense and CIS", Pp. 218, 2014.

[18] Zhang, J.C., Z.Y. Xu, Z.Y., Zhu, D., Su, W.F., Zhu, D. (2016). Study of tool trajectory in blisk channel ECM with spiral feeding. Mater Manuf Process. Vol. 32. Pp. 333–338. doi: https://doi.org/10.1080/10426914.2016.1151040

[19] Zhu, Z.W., Wang, D.Y., Bao, J., Zhu, D. (2015). Process simulation of electrochemical machining of convexity structure on revolving workpiece. The ASME 10th International manufactures science and engineering conference. 2015. doi: 10.1115/MSEC20159275

[20] Lazarov, R. (2024). Research on the change in ballistic characteristics of ammunition with a modified projectile shape during its movement in an air environment. Environment. Technologies. Resources. Proceedings of the International Scientific and Practical Conference. Vol.4. Pp. 164-167. doi: https://doi.org/10.17770/etr2024vol4.8194

[21] Li, X., Wang, Y., Zang, Y., Guan, B., Qin, Q. (2019). Analysis of interior ballistic performance degradation of a worn gun barrel based on finite element method. Journal of Physics: Conference Series. Vol.1314 doi: 10.1088/1742-6596/1314/1/012090

[22] Trebinski, R., Fikus, B., Surma, Z. (2017). Investigations of Ballistic Characteristics of N340 Propellant. Problems of Mechatronics Armament Aviation Safety Engineering. Vol. 8. Pp. 9-22. doi: 10.5604/01.3001.0010.7314

[23] Abaci, W. B., Hristov, N., Ahmed, N. Z., Jerkovic, D., Drakulic, M. (2022). Determination of the gun barrel walls temperature distribution and its experimental validation during multiple-shots firing process. International Journal of Thermal Sciences. Vol. 179 doi: https://doi.org/10.1016/j.ijthermalsci.2022.107667

[24] Conev, C., Karadzhov, T. (2023). Application of the Finite Element Method for the Design of Small Arm Barrels. Environment. Technology. Resources. Proceedings of the 14th International Scientific and Practical Conference. Vol. 2. Pp. 114-118. doi: https://doi.org/10.17770/etr2023vol2.7213

[25] Cheng, Q., Yang, G., Yu, C., Sun, Q. (2017). The modal analysis of three-dimension gun barrel using isogeometric analysis and its application to optimization. Journal of Vibroengineering. Vol. 19. Pp. 6277–6287. doi: 10.21595/jve.2017.18897

[26] Shuqiang, G., Mingmin, L., Feng, X. (2022). Strength and Modal Analysis of a Gun Barrel under Four Different Strength Theories. Journal of Physics: Conference Series. Vol. 2460. doi: doi:10.1088/1742-6596/2460/1/012058